Submicron hollow spot generation by solid immersion lens and structured illumination



2012 New J. Phys. 14 103024

(http://iopscience.iop.org/1367-2630/14/10/103024)

New Journal of Physics
The open-access journal for physics

# Submicron hollow spot generation by solid immersion lens and structured illumination

**M-S Kim[1,4], A C Assafrao[2], T Scharf[1], A J H Wachters[2], S F Pereira[2], H P Urbach[2], M Brun[3], S Olivier[3], S Nicoletti[3] and H P Herzig[1]**

[1] Optics and Photonics Technology Laboratory, Ecole Polytechnique Fédérale de Lausanne (EPFL), Rue A-L Breguet 2, Neuchâtel CH-2000, Switzerland
[2] Optics Research Group, Delft University of Technology, Lorentzweg 1, 2628 CJ Delft, The Netherlands
[3] CEA-LETI, Minatec Campus, 17 rue des Martyrs, 38054 Grenoble Cedex 9, France
E-mail: myunsik.kim@epfl.ch

*New Journal of Physics* **14** (2012) 103024 (19pp)
Received 13 June 2012
Published 16 October 2012
Online at http://www.njp.org/
doi:10.1088/1367-2630/14/10/103024

**Abstract.** We report on the experimental and numerical demonstration of immersed submicron-size hollow focused spots, generated by structuring the polarization state of an incident light beam impinging on a micro-size solid immersion lens ($\mu$-SIL) made of $SiO_2$. Such structured focal spots are characterized by a doughnut-shaped intensity distribution, whose central dark region is of great interest for optical trapping of nano-size particles, super-resolution microscopy and lithography. In this work, we have used a high-resolution interference microscopy technique to measure the structured immersed focal spots, whose dimensions were found to be significantly reduced due to the immersion effect of the $\mu$-SIL. In particular, a reduction of 37% of the dark central region was verified. The measurements were compared with a rigorous finite element method model for the $\mu$-SIL, revealing excellent agreement between them.

[4] Author to whom any correspondence should be addressed.

## Contents



## 1. Introduction

By manipulating the state of polarization of a laser beam, structured focal spots can be generated in the focal plane of an optical system. In particular, when a cylindrical vector beam is incident on a focusing lens of relatively low numerical aperture (NA), a doughnut-shape focused spot is generated. Typically, a radially or azimuthally polarized light leads to such doughnut-shape hollow spots [1, 2]. The former type of cylindrical polarization, namely radial polarization, has attracted much attention of researchers owing to the presence of a strong longitudinal component for high-NA focusing lenses. This strong longitudinal field component fills up the central dark zone of the doughnut beam and finally generates a sharper focus compared with that of a linear polarization with the same NA lens in theory [3, 4]. A reduced bright focal spot finds its application in many research areas ([5, 6] and references therein): not only in fundamental subjects such as microscopy, lithography and optical data storage systems, but also in advanced research, for instance, Raman spectroscopy, particle acceleration, fluorescent imaging and second- or third-harmonic generation. The latter case, the pure hollow spot created by focusing an incident azimuthally polarized light, is equally advantageous for many other super-resolution optical systems, such as stimulated emission depletion (STED) microscopy [7] and subdiffraction lithography [8, 9]. Another fascinating application is optical trapping, where the central dark zone of the doughnut spot is essential to trap and manipulate tiny objects that might be repelled and pushed away from the regions of maximum intensity [10]. Low-refractive-index particles, such as air bubbles in liquids and metallic particles at certain frequencies, are typically repelled by a bright spot [11, 12]. Absorbing (i.e. non-transparent) particles in liquids and a gaseous medium are also repelled and pushed away from intensity maxima [13–15]. In particular, a dark trap is more beneficial for some applications than a bright trap for a simple reason: the light may not interact with the trapped object. This is of great advantage while trapping photosensitive materials, e.g. biological cells, and for trapping neutral atoms [16–18].

Although optical trapping has been demonstrated using radial polarized beams, the strong longitudinal field component creates major difficulties when the aforementioned particles are considered. In contrast, when focusing an azimuthally polarized light, a dark central zone is always achieved due to non-existence of a longitudinal field, regardless of the NA of the focusing lenses employed [1, 2, 19]. Such remarkable characteristics, i.e. a doughnut focused spot with a well-defined dark zone, is by itself a major improvement on dark optical trapping techniques. A further improvement step can be achieved by diminishing the overall size of the dark region, which would immediately allow for trapping even smaller samples. Such an attempt at nano-particle dark trapping has recently been reported using plasmonic nano-antennas [20].

Since most optical systems are already operating at high NAs, diminishing the size of the dark region demands that the NA should be pushed beyond the unity limitation. In this work, a detailed study of the doughnut-shaped focal spot, generated with azimuthally polarized laser beams, is given for a high-performance optical system with an NA larger than unity. To achieve such a high NA, a micro-size solid immersion lens ($\mu$-SIL) is placed in the focal plane of an NA $= 0.9$ focusing lens. The resulting structured immersion focal spot is then measured with a high-resolution interference microscope (HRIM), which allows measuring light fields with nanometer precision. The experimental data are compared with a rigorous three-dimensional (3D) computational model, based on the finite element method (FEM) that simulates the electric field distribution in the vicinity of a 2 $\mu$m diameter SIL. Comparisons between the experiments and simulations are made, revealing good overall agreement. The remainder of this paper is organized as follows. In section 2, methods for achieving NA larger than unity are briefly discussed. In section 3, the experimental arrangements for realizing the cylindrically symmetric polarization status, especially azimuthal polarization, are shown. Next, in section 4, the fabrication and geometry of the $\mu$-SIL are described. Section 5 is dedicated to the experimental exploitation of the principal responses of the $\mu$-SILs, namely spot-size reduction and peak intensity enhancement. In section 6, the rigorous 3D FEM simulation model for $\mu$-SIL is presented. Finally, in section 7, the actual measurements of the structured focused spots generated by the $\mu$-SIL, along with the simulation results, are shown. The conclusions are presented in section 8.

## 2. Immersion technique

When focusing light through a medium made exclusively of air, the maximum achievable NA is theoretically limited to unity. This limitation follows directly from the definition of NA, given by

$$\mathrm{NA} = n \sin\theta. \tag{1}$$

Here, $\theta$ is the angle that the marginal ray makes with the optical axis (half-angle of the focusing cone) and $n$ is the refractive index of the medium through which the rays pass. Therefore, a straightforward solution to increase the NA is to switch the working space medium from air to a higher-refractive-index material. In other words, the utilization of an immersion technique can push the NA barrier above unity. Figure 1 illustrates the working principle of liquid and solid immersion schemes. When one simply inserts a high-refractive-index medium with a planar surface in an attempt to increase the NA by a factor of $n$, refraction of light reduces the focusing angle $\theta$ to $\theta'$, according to Snell's law. This situation is depicted in figure 1(b). A quick analysis using equation (1) and Snell's law leads to the conclusion that the NA is sustained as before.

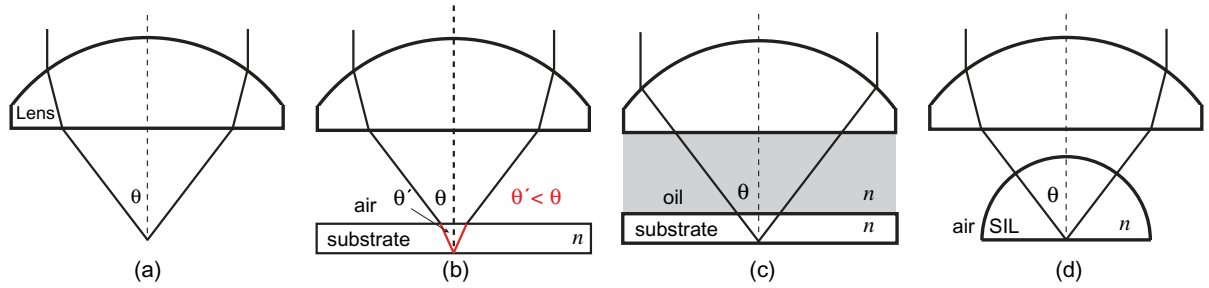


**Figure 1.** Working principle of the liquid and SIL techniques. All figures depict a light ray being focused: (a) in air, (b) through a substrate with a planar interface, (c) throughout liquid immersion by oil and (d) onto a solid immersion with a hemispherical solid medium. The NA is the product of the refractive index $n$ and the sine of the half-focusing angle $\theta$, $\mathrm{NA} = n \sin\theta$.

This can be understood by noting that the tangential components of the wave vector are the same on both sides of the interface. Hence, the spatial frequencies are also the same. Moreover, the quality of the focus is actually degraded by spherical aberrations introduced by the substrate, due to multiple reflections and refraction of light at the substrate–air boundaries [21]. Thus, a single planar substrate is not always the best solution for the immersion technique. A more efficient immersion approach is achieved by filling the air gap between the planar substrate and the focusing lens with a material having the same refractive index as the substrate. In the history of optics, it was Hooke who first discussed such an immersion technique to improve the imaging performance in microscopy [22]. This homogeneous immersion concept was pushed forward by Abbe, who was able to construct the first oil-immersion lens when setting up the imaging theory of microscopy [23]. In a homogeneous immersion concept, oil serves as a perfect index matching medium for the coverglass plate, so that complete homogeneity is obtained, as shown in figure 1(c). Note that now there is no additional refraction on the planar interface of the substrate. As a consequence, the NA is increased by a factor equal to the refractive index $n$ (see equation (1)), with the major benefit of avoiding all aberrations generated by the planar interface substrate.

In 1990, a new immersion technique was introduced by Mansfield and Kino [24]. Instead of filling the air gap with a liquid medium, an SIL is placed in the focal plane of the focusing objective, as illustrated in figure 1(d). Hence, when the light is focused on the center of the hemispherical solid lens, the light rays will always be normally incident with respect to the spherical interface. This avoids the additional refraction at the interface between air and the solid medium. Such a solid immersion technique also increases the effective NA by a factor of $n$, in a similar way to liquid immersion. The main advantage of the SIL lies in the fact that no liquid is needed in this configuration and that more materials with a higher refractive index are available in a solid state. This broadens the range of immersion microscopy applications. For a long time, the fabrication of SILs was limited to macro-size, i.e. millimeter range dimensions, due to the lack of advanced fabrication technologies. The recent advance in micro- and nano-technology boosted the development of different types of SILs, for instance, diffractive SILs [25], $\mu$-SILs [26–28], nano-size SIL-like elements [29, 30] and subwavelength-size SILs [31]. These new types of $\mu$-SILs open an entirely new research field in which the optical characterization of the focused field generated by such SILs is a challenging task. This is one of our primary goals

in this paper. We will study a micro-fabricated hemispherical SIL, having 2 $\mu$m diameter and a body filled with $SiO_2$ [28]. In section 3, a short description of the high-resolution interference microscope is given, along with the experimental conditions for generating structured focused beams.

## 3. Experimental arrangement

### *3.1. Experimental setup*

For measuring the immersion focused field generated by the $\mu$-SIL, an HRIM is employed. The HRIM technique has been proven to be a powerful tool for 3D optical characterizations of macro-, micro- and nano-optical elements [32–34] and to measure light field features with nanometer precision [35]. Even if the interferometric function is not essential in this study, the auxiliary functions facilitate to characterize such small SILs (diameter 2 $\mu$m) and to manipulate the polarization of the illumination for the beam shaping. In figure 2, a schematic diagram of the experimental setup is displayed. A single-mode polarized laser diode (CrystaLaser, 642 nm: DL640-050-3) is employed as a light source. The laser light is expanded and collimated by a spatial filtering technique, being redirected to the object arm of the microscope. Even though not used in the present study, the reference arm is also shown. For the complete descriptions of the HRIM experimental setup, see [30–32]. An objective lens of NA = 0.9 is used to focus the normally incident $x$-polarized plane wave. The objective is mounted on a precision piezo stage with a $z$-scan range of 500 $\mu$m and an $x$–$y$ scan range of 100 $\mu$m (Mad City Labs). Whenever necessary, additional optical elements are introduced along the optical path in the reserved squares 1 and 2, as indicated in the figure. The $\mu$-SIL will be later positioned in the focal plane of the focusing objective, also on the piezo stage. As seen, the measurements are made in transmission.

### *3.2. Focused spots of structured illumination*

In order to manipulate and structure the incoming collimated beam, additional optical components are introduced in the reserved squares 1 and 2, as indicated in figure 2. Usually, a radial/azimuthal polarization converter is introduced in square 1, whereas an annular aperture or an additional linear polarizer is placed in the position indicated by square 2. In theory, the polarization status of the cylindrical vector beams can be visualized by using the higher-order Poincaré sphere [36, 37]. The cylindrically symmetric polarization status is achievable by using computer-generated holograms, a spatial light modulator, subwavelength gratings, segmented half-wave plates (for a good review of different methods, see [1]). In our study, we employ a liquid-crystal polarization convertor [38] from ARCoptix. This manipulates the polarization of the incident collimated beam from linear to radial or azimuthal depending on the twisted nematic cell, which rotates the direction of the linear polarization by 90°. As discussed before, focusing such a beam of cylindrically symmetric polarization with a low-NA lens results in the desired doughnut-shaped, vector Laguerre–Gaussian [1, 2], focused spot. While the radial polarization ensures the doughnut beam only when a low-NA focusing lens is applied, the azimuthal polarization always generates the dark zone (i.e. null intensity) in the center of the focal spot, regardless of the NA of the focusing lens. Therefore, the latter polarization is preferred for advanced optical systems in which high-NA lenses are employed to generate the

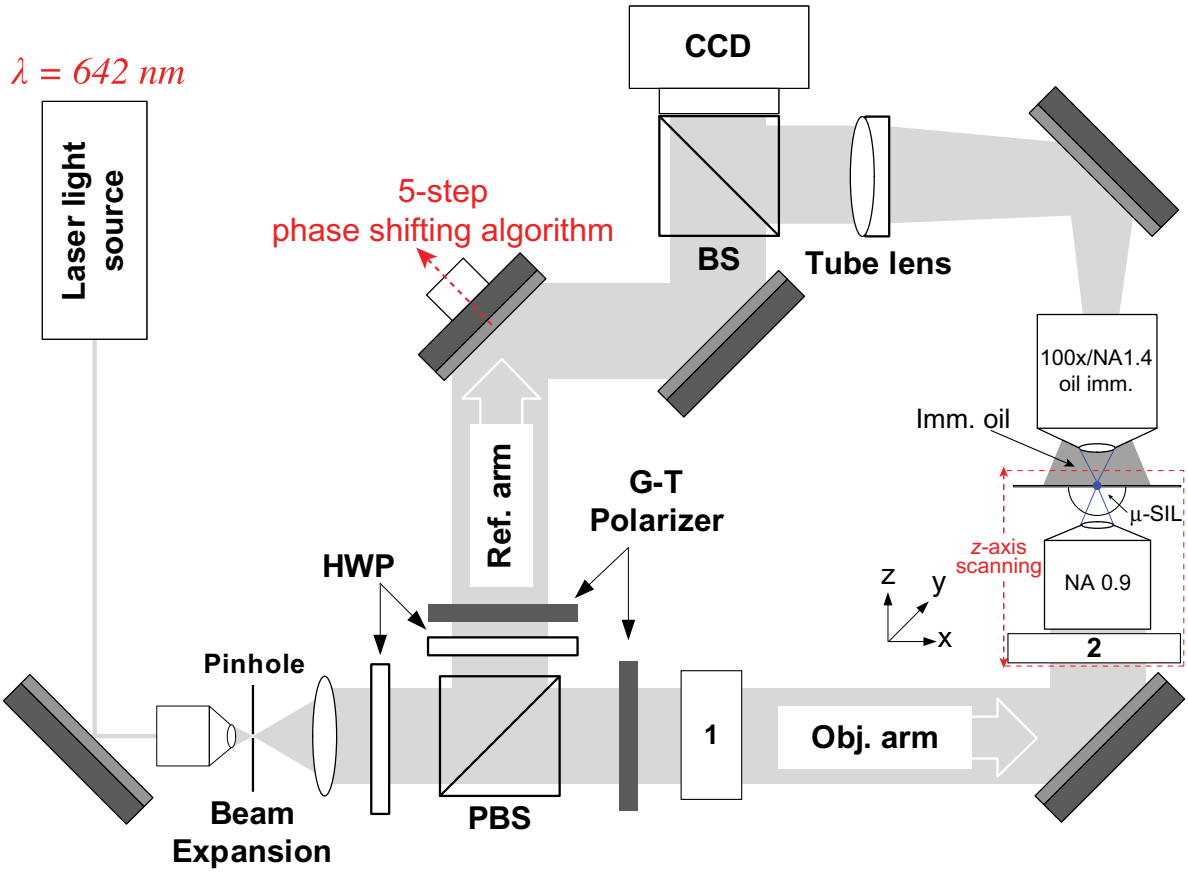


**Figure 2.** Schematic diagram of the experimental setup of the HRIM. The $\mu$-SIL and the NA = 0.9 focusing lens are inserted on the same sample stage. In the object arm, a plane wave is normally incident onto the focusing lens. By scanning the $\mu$-SIL together with the focusing lens along the $z$-axis, 3D maps of the focused field are obtained. Additional optical elements are introduced in squares 1 and 2 to manipulate the wavefront and polarization state of the light.

hollow spots. Hence, throughout this work, this particular state of polarization shall be used. In figure 3, when immersion is not yet applied, the four different structured focal spots measured are shown. The spot shown in figure 3(a), measured in the focal plane of the NA = 0.9 lens, is obtained by focusing the incident azimuthally polarized beam without any other optical elements in square 2. Note that the desired doughnut shape, with a pronounced dark zone in its central region, is obtained under these experimental circumstances. If a linear polarizer with extinction axes in the transverse plane is now introduced in the position indicated by square 2, the doughnut beam is decomposed into a two-half-lobes spot, as shown in figures 3(b) and (c). When the linear polarizer is removed and an annular aperture, which blocks 70% of the entrance pupil of the focusing lens, is inserted in square 2 position, the amplitude distribution of the focused spot in the focal plane resembles the first-order Bessel function of the first kind, as shown in figure 3(d). This type of experimental beam is known as the *Bessel–Gauss beam* for both a scalar field [39] and a vector field [40, 41]. Our result in figure 3(d) fails in the case of a

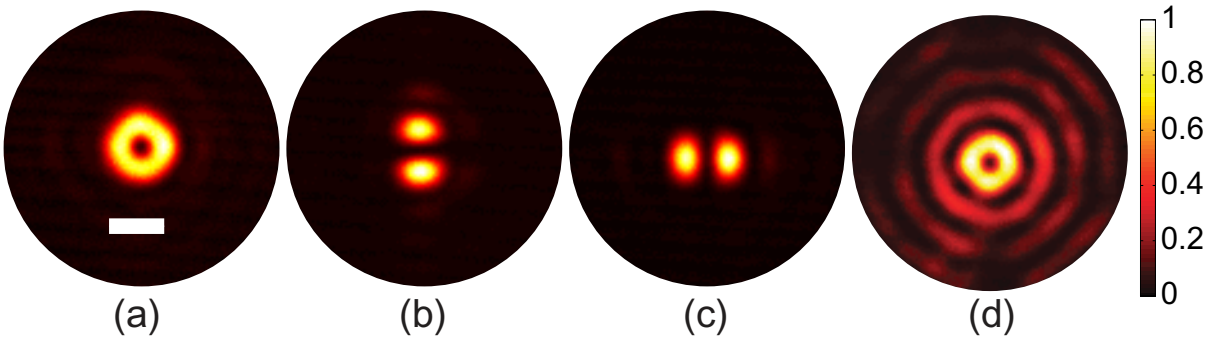


**Figure 3.** Measured transverse intensity distributions of the structured non-immersed focal spots generated by the NA = 0.9 objective. The incoming plane wave is azimuthally polarized. (a) No additional optical elements are introduced. A typical doughnut-shaped spot is obtained. A linear polarizer is used to decompose the azimuthally polarized beam, resulting in the two-half-lobes spots with the extinction axis parallel to (b) the $x$-axis and (c) the $y$-axis, respectively. (d) The first-order Bessel–Gauss spot generated by introducing an annular aperture at the entrance pupil of the focusing lens. A dark central zone is also obtained for this case. The scale bar represents 1 $\mu$m. The intensities are all normalized.

vector field due to the high-NA focusing. Nevertheless, a tiny central dark zone is also observed in this type of focused spot at the cost of stronger side lobes.

At this point, experimental procedures for obtaining structured focused spots at high NA, characterized by the desired doughnut shape, are described. The next step is, therefore, to study the immersion properties of these particular spots under a $\mu$-SIL influence. Thus, in section 4, a brief discussion of the $\mu$-SIL geometry is presented, followed by an immersion study.

## 4. Geometry of the micro-size solid immersion lens

In this study, a chip containing many hemispherical $\mu$-SILs, having 2 $\mu$m diameter, is employed. The fabrication of such $\mu$-SILs is a result of several conventional micromachining processes combined, such as etching, deposition and polishing. The details of the fabrication processes are reported in [28]. In figure 4, the geometry of a single $\mu$-SIL is shown. The hemispherical SIL body, filled with silicon dioxide ($SiO_2$, $n = 1.5$), is held by a 200 nm thick silicon nitride ($Si_3N_4$) membrane of $100 \times 100\,\mu m^2$. The main SIL chip is formed in a 550 $\mu$m thick silicon (Si) substrate, which is back-side etched to release the spherical surface to the air. Note that side wall angle $\alpha$ of the Si substrate and the 100 $\mu$m width of the bottom opening lead to the back-side opening of approximately 1.65 mm. By simply applying geometrical optics, one can conclude that the size of the NA = 0.9 focused beam 550 $\mu$m above the focal plane will be larger than this opening itself, therefore limiting the NA of the focusing lens. In fact, the finite size of this back-side opening results in an effective NA of approximately 0.8. The $\mu$-SILs are designed in an array with various numbers, e.g. $3 \times 3$, $2 \times 2$ and $1 \times 6$, and a single SIL as well. Since the thin $Si_3N_4$ membrane is transparent for the visible spectrum, the $\mu$-SILs can still be seen from the bottom surface side and localized through the membrane. In this way,

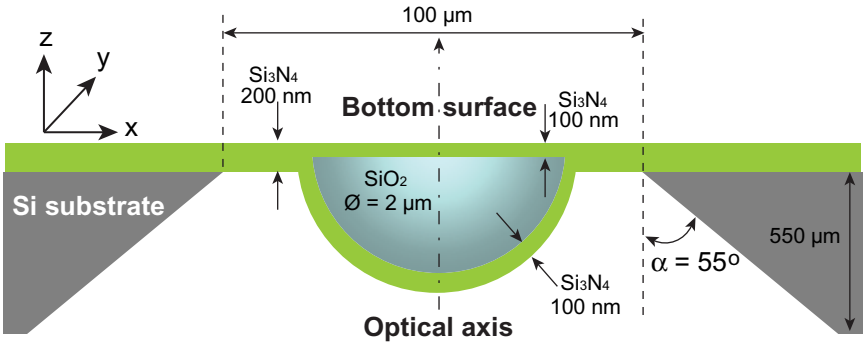


**Figure 4.** Schematic representation of the $\mu$-SIL geometry: the hemispherical SIL body ($SiO_2$) with 2 $\mu$m diameter is held by the 200 nm thick $Si_3N_4$ membrane. The thickness of the Si substrate is 550 $\mu$m and the side wall angle $\alpha$ is approximately 55°. The width of the bottom opening is 100 $\mu$m (not to scale here). Light propagates along the positive $z$-axis.

optical characterizations are carried out through this membrane in the HRIM, as explained in figure 2.

## 5. Verification of the immersion effect

The expected property of the $\mu$-SIL is, naturally, to reduce the focal spot size by a factor intrinsically related to the refractive index of the immersion medium. As a primary consequence, the resolution of the optical system in which the $\mu$-SIL is employed would be increased. In this section, a preliminary experimental investigation of the spot-size reduction caused by the $\mu$-SIL is carried out. For the moment, no additional optical components (polarization converters, annular aperture, etc) are used in the optical setup. Therefore, the incident illumination upon the objective lens is the collimated linearly polarized plane wave. Figure 5 shows the observed focal spots on the bottom of the SIL chip, where the $Si_3N_4$ membrane holds the $\mu$-SILs (see figure 4).

The $3 \times 3$ circular features represent the bottom view of the 2 $\mu$mSILs. Initially, a reference spot is defined by focusing the light onto the $Si_3N_4$ membrane (out of the SIL), as shown in figure 5(a). This spot is referred to as a non-immersed spot. Next, the light is focused onto each of the $\mu$-SILs at a time, as shown in figures 5(b)–(h). Visually, it is already possible to recognize the spot-size reduction and the intensity enhancement due to the expected immersion effect. Moreover, a rough inspection of the immersed spot size indicates that all lenses respond to the incident field in a similar way. This gives an indication of the uniformity and homogeneity of the fabricated $\mu$-SILs.

Further quantitative analysis has been carried out on the measured data in order to confirm the aforementioned observations. For a statistical analysis, each spot has been measured five times at the same position. The results indicate that the transverse size of the non-immersed focused spot is $502 \pm 10$ nm along the $x$-axis and $504 \pm 9$ nm along the $y$-axis. In the longitudinal direction, i.e. along the $z$-axis, the spot size and the peak intensity are found to be $3805 \pm 39$ nm and $115 \pm 4$ (arbitrary unit), respectively. The small standard deviation values for the spot size ($<2\%$) confirm the repeatability and reliability of our measurements. For the immersed spots, the standard deviation from the five measurements exhibits analogous results to that of the

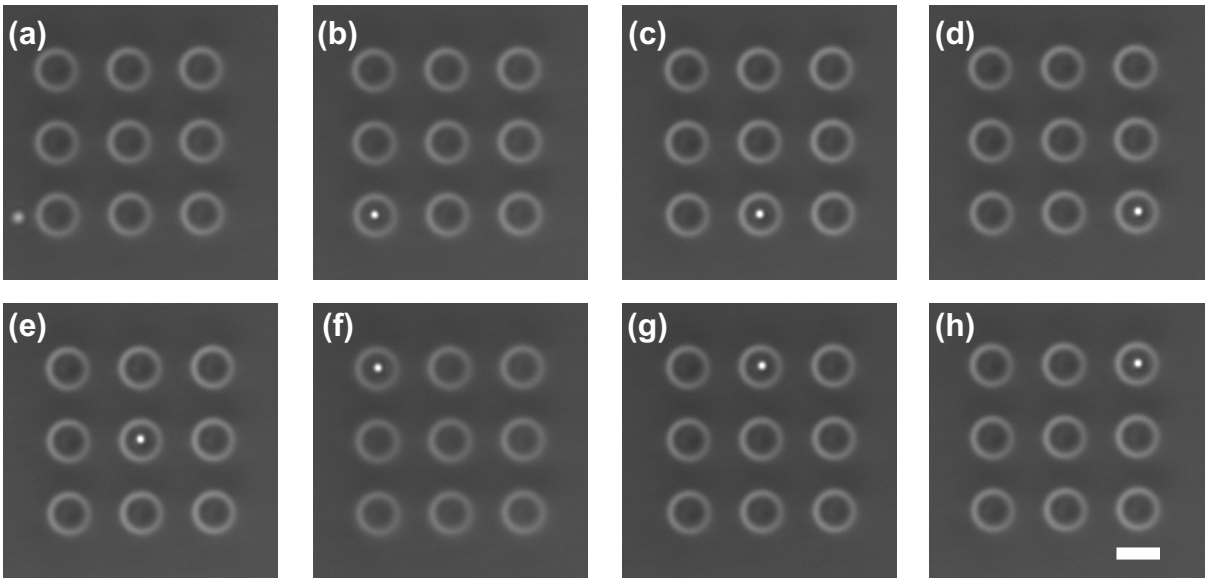


**Figure 5.** Focal spots observed on the bottom of the SIL chip, where the $3 \times 3$ circular features represent an array of $\mu$-SILs. (a) The focal spot outside the $\mu$-SIL (non-immersion spot) and (b)–(h) the focal spots on the individual $\mu$-SIL (immersion spots). The image size is $15 \times 15\,\mu\text{m}^2$ and the scale bar represents $2\,\mu$m.

non-immersed spot. Taking, for example, the spot shown in figure 5(d), the transverse size is $343 \pm 6$ nm in the $x$-axis and $350 \pm 7$ nm in the $y$-axis. Along the $z$-axis, the peak intensity is $204 \pm 8$ (arbitrary unit) and the spot size is $1392 \pm 63$ nm. A direct comparison of the average transverse size of the non-immersed and the immersed focal spots shows a reduction ratio of approximately 1.5 ($x$-axis: 1.47 and $y$-axis: 1.4). This agrees with the refractive index value of the $SiO_2$ SIL, namely $n = 1.5$ at 642 nm wavelength. The peak intensity is enhanced by the immersion effect, due to stronger spatial confinement of light. Considering the power $P$ carried by a Gaussian beam, expressed by equation (2), an estimate of the peak enhancement can be derived:

$$P = \tfrac{1}{2}\pi w^2 I. \tag{2}$$

Here, $I$ is the peak intensity and $w$ is the beam waist [42]. Note that equation (2) is valid for a scalar field. For the vector field, the beam waist $w$ along the $x$- and $y$-axes should be taken into account. However, equation (2) provides a quick estimation of the peak intensity enhancement caused by the immersion effect. For the case of no absorption and other losses (i.e. $P$ is a constant), the peak intensity value is only proportional to the square of the spot size. The spot-size reduction of 1.5 theoretically leads to the peak intensity enhancement of $2.25 (= 1.5^2)$. In the measurements, the peak intensity is enhanced by a factor of 1.87. This roughly indicates that there is a transmission loss of approximately 17% that includes the 13% reflection loss at the spherical surface. In conclusion, the spot-size reduction due to the $\mu$-SIL is found to be of the same order as the refractive index of the material of the lens. These results, which hold for $x$-polarized light, must now be investigated for the structured illumination beams having azimuthal polarization. The next sections are, therefore, exclusively dedicated to study such structured spots.

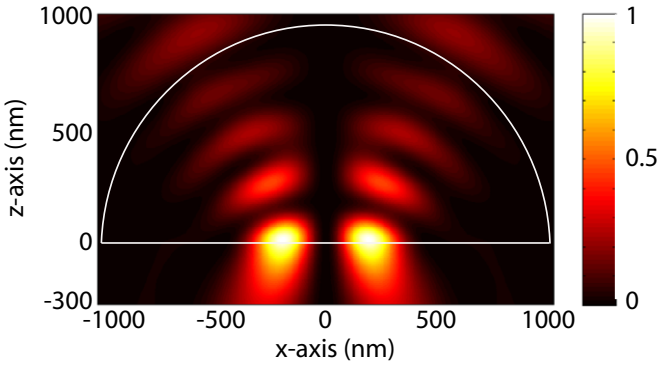


**Figure 6.** Computational domain of the 3D FEM model for the $\mu$-SIL. The $\mu$-SIL, described as a hemihemispherical structure, is placed in the focal plane of an objective lens with an effective NA of 0.8. The immersed focal spot, collected at the bottom of the $\mu$-SIL lens, will be used for comparison with the measurements.

## 6. Rigorous simulation model for micro-size solid immersion lens

The small features of the $\mu$-SIL introduce extra concern when one tries to rigorously simulate the focused spot generated by these tiny SILs. Unlike the models used to describe an SIL, which usually consider an upper half-space filled with the refractive index of the SIL material, the wavelength dimensions of the $\mu$-SILs require a complete meshing representation of the SIL structure. In a sense, the $\mu$-SIL must be treated as a small scatterer, whose shape, size and orientation cannot be neglected. Since this scatterer is placed on the focal plane of a high-NA focusing lens, the vectorial nature of the light must also be taken into account. Hence, a rigorous simulation tool, based on solving Maxwell's equations and capable of handling complicated structures, has to be applied when analyzing such problems. Therefore, throughout this work, all simulations described are carried out in a rigorous 3D FEM simulation tool [43, 44].

In a typical simulation section, the polarized laser light (at the wavelength of 642 nm) is focused onto the planar bottom surface of the $\mu$-SIL, as shown in figure 6. Note that light propagates from the top to the bottom. The geometrical focus of the high-NA lens is chosen to be at $z = 0$ nm, coincident with the bottom of the $\mu$-SIL. The $\mu$-SIL is meshed as a 3D hemispherical object with refractive $n = 1.5$. All surrounding space is filled with air ($n = 1$). A higher number of points in the central region of the computation domain were assigned to ensure good representation of the rounded $\mu$-SIL structure. All simulations were performed in a cluster of four AMD Quad-Core Opteron 6176 (2.3 GHz) with 256 GB of internal memory, operating under the Linux environment. Elements of order 2 [45] were used on a hexahedral mesh with total size varying from $2100 \times 2100 \times 1350\,\text{nm}^3$. The mesh size was chosen in such a way that the entire $\mu$-SIL fits completely inside the computational domain, a condition necessary for achieving convergence. A perfect matched layer [45] with a width of 50 nm in all directions was defined to truncate the computational domain. The total execution time of a single calculation was about 6 h. In figure 6, the normalized energy density of the total electric field, i.e. $|E_t|^2 = |E_x|^2 + |E_y|^2 + |E_z|^2$, computed across the $\mu$-SIL is shown. Here, $E_x$, $E_y$ and $E_z$ are the complex electric field components and $E_t^2$ is usually referred to as the total electric field or field intensity $I$. From the normalized form of the total electric field intensity, computed

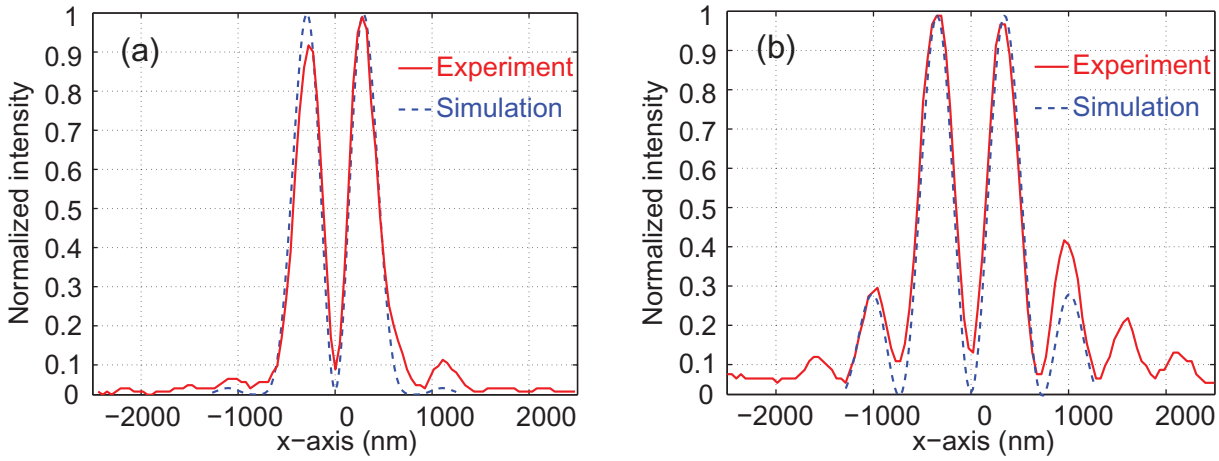


**Figure 7.** Intensity profiles of the measured and simulated non-immersed structured focal spots: (a) the doughnut-shape hollow spot (see figure 3(a)) and (b) the first-order Bessel–Gauss focal spot (see figure 3(d)). Excellent agreement is found between experiments and simulations. The intensities are all normalized.

below the boundary (SIL–air), the spot profile is taken and will be used for comparisons with the experimental data.

When the $\mu$-SIL is removed from the computational domain, the focused spot generated by the focusing objective lens alone must match the measured spot shown in figure 3(a). Therefore, a preliminary simulation for the azimuthally polarized beam being focused by an NA $= 0.8$ lens (considering the NA cut-off due to the finite size of the Si substrate opening, see section 4), with and without the annular aperture, is performed and compared with the measured spots. The results are plotted in figure 7. When the azimuthally polarized beam is focused by the high-NA objective, the doughnut-shaped spot is obtained in the focal plane, as seen from the profile shown in figure 7(a). The blue dashed line, obtained from the simulation, is in good agreement with the measured spot under the same conditions (red solid line). In the same way, when an annular aperture is placed in front of the focusing objective, the resulting first-order Bessel–Gauss is realized. The polarization of this generated Bessel–Gauss beam is azimuthal, which leads to a cylindrically symmetric focal spot. The vector nature of the highly focused field causes the depolarization effect [46], which decomposes the polarization into the *xyz* components. However, the azimuthal polarization naturally possesses only the transverse components, i.e. the *xy* ones. Therefore, the generated first-order Bessel–Gauss beam exhibits the central null intensity with relatively strong side lobes. As shown in figure 7(b), good agreement is also obtained between experiment and simulation in this case. Hence, the next step is to place the $\mu$-SIL on the focal plane of the high-NA lens in order to study numerically and experimentally the structured immersed focused spots.

## 7. Structuring immersion focal spots

As previously discussed, different optical elements are introduced in the optical path of the laser beam leading to the structured focal spots, such as the desired doughnut-shaped spot. Now, the structured focused spots are immersed using the $\mu$-SIL. The measured spots are

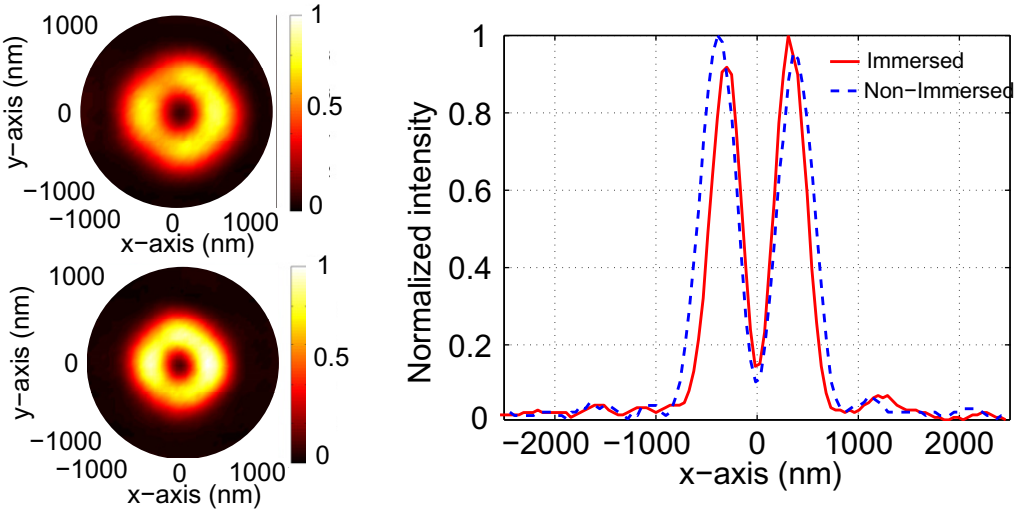


**Figure 8.** Measured intensity distributions of the doughnut-shape hollow spots: top left, the non-immersed spot is mapped in a 2 $\mu$m circular measuring window. The immersed spot is shown bottom left. The intensities are normalized with respect to the peak intensity of the immersion spot. In the right figure, the profiles along the $x$-axis for both spots are plotted after unity normalization. A reduction of the spot size of approximately 30% is achieved due to the immersion lens.

then qualitatively and quantitatively compared with the simulation results, for the doughnut spot, the two-half-lobes spot (the decomposed case of the doughnut spot) and the first-order Gauss–Bessel spot.

### *7.1. Doughnut beam by focusing azimuthal polarization*

The first case considered is the azimuthally polarized laser beam being focused by the high-NA lens onto and outside the $\mu$-SIL. The measured immersed and non-immersed focal spots are mapped in a circular measuring window with 2 $\mu$m diameter, after being normalized by the maximum intensity value of the immersed spot. The figure color map is adjusted to display colors from zero to unity in both figures in such a way that the difference between maximum intensities can be readily visualized. To quantify the measured spots, the unity normalized intensity profiles along the $x$-axis are also plotted. The results are shown in figure 8. From the focused spot intensity distributions shown on the left, it is qualitatively visible that spot-size reduction occurs due to the immersion effect. Moreover, by comparing the maximum intensity values in both immersed and non-immersed spots, it is found that the measured peak intensity of the immersed spot is enhanced by 1.54 times compared with the non-immersed one. On the right plot, the intensity profiles quantitatively show an overall reduction in the immersed spot size and the size of the central dark region, measured in terms of the full-width at half-maximum (FWHM). On average, the immersed focused spot is reduced by a factor of 1.3 times compared with the non-immersed spot. In what follows, a further comparison with the simulations is made.

The simulation is carried out as explained in the previous section. The azimuthally polarized light is focused onto and outside the $\mu$-SIL, and the spot computed in the radial direction (i.e. $x$- and $y$-directions) is plotted as a function of the position. The same color-map

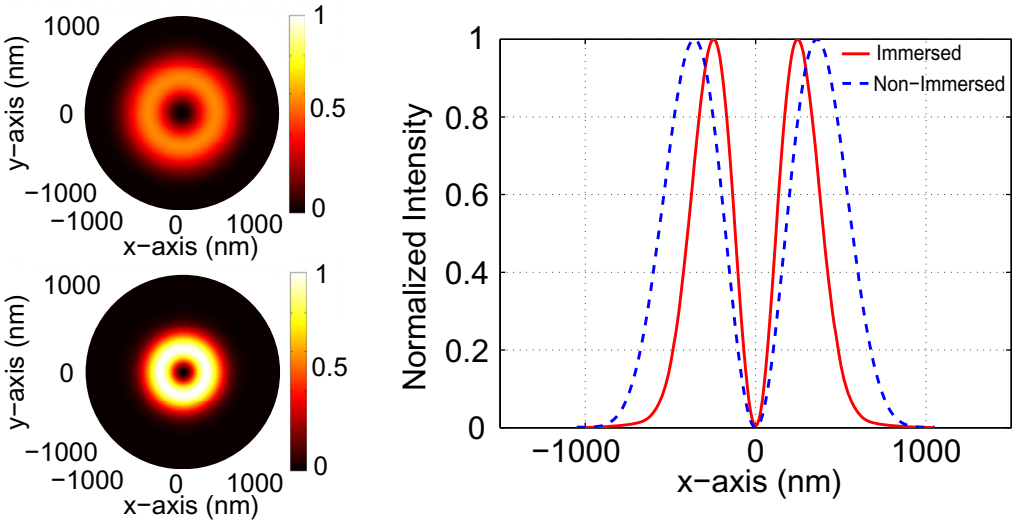


**Figure 9.** Simulated intensity distributions of the doughnut-shape spots: top left, the non-immersed doughnut spot is mapped in a 2 $\mu$m circular measuring window. The simulated immersed spot is shown bottom left. The intensities are normalized in the same way as in figure 8. A peak intensity enhancement of 2.48 due to the immersion effect is found. On the right, the profiles along the $x$-axis for both spots are plotted after unity normalization. The immersed spot size is reduced by a factor of 1.5 compared with the non-immersed spot. This value corresponds to the refractive index of the $\mu$-SIL body.

standard as in figure 8 is applied here for the immersed and non-immersed spots. In addition, the intensity profiles taken along the $x$-direction are also provided. The results are shown in figure 9. A quick comparison with the measured spots reveals the same type of doughnut-shaped focused spot for both the immersed and the non-immersed cases. Moreover, the peak intensity of the immersed spot is higher than that of the non-immersed spot, as a result of light confinement due to the immersion lens. For the immersion spot, the peak intensity is increased by a factor of 2.23 and the FWHM size reduction ratio of the outer rim of the doughnut shape is approximately 1.48(= 920 nm/620 nm), which is close to the refractive index of the $SiO_2$ SIL ($n = 1.5$).

For optical dark trapping and STED-like lithography, the central dark spot is certainly the most important feature in the structured focused spot. Hence, a careful analysis of that region revealed that the FWHM size of the dark spot is reduced from 300 to 220 nm in the presence of the $\mu$-SIL. This corresponds to a reduction ratio of 1.37, slightly smaller than the lens refractive index. By simply applying geometrical optics approximation to analyze the problem, one would expect an overall spot-size reduction ratio equal to the refractive index of the SIL. However, since the vector nature of the light starts to play an important role at subwavelength problems, such an approximation does not hold anymore. Thus, these observations show the importance of using rigorous Maxwell's equation solvers to analyze complex optical problems.

In figure 10, a direct comparison between the intensity profiles of the measured and simulated immersed doughnut-shape focused spots is shown. As seen in the figure, the outer rim of the measured doughnut spot is slightly broader than that of the simulated counterpart. This difference is most likely to be due to deviations of the lens from the ideal half-spherical

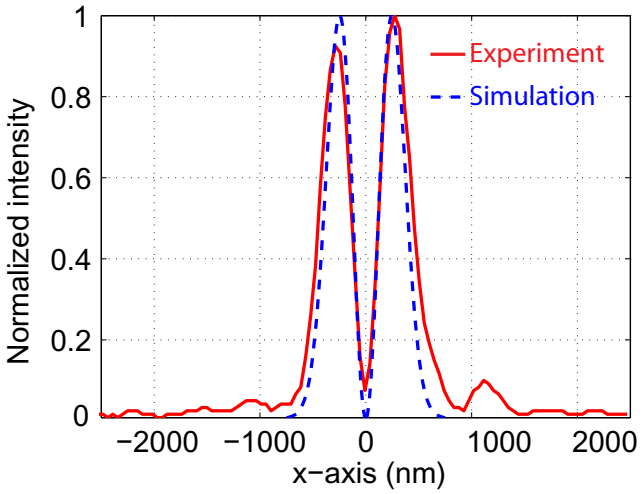


**Figure 10.** Comparison between the measured and the simulated intensity profiles of the immersed doughnut spot. The measured central dark region shows good agreement with that of the simulation. All intensities are normalized.

shape, which is expected to be more pronounced on the outer regions of the $\mu$-SIL. Thus, since the full extension of the incident doughnut spot on the $\mu$-SIL reaches up to 2 $\mu$m (see figure 7), a larger deviation from the ideal case (simulation) will occur in that region. In addition, not including the $Si_3N_4$ layer and the Si holder structure in the simulation model may also be contributing to the small difference. On the other hand, the central dark regions of both the measured and the simulated spots show excellent agreement. The reason is, as seen from the performance test of the immersion effect done with the linearly polarized plane wave, that the central part of the $\mu$-SIL has a much better spherical surface, thus minimizing the experimental errors in that region.

### *7.2. Decomposed azimuthal polarization: the two-half-lobes spot*

A second interesting type of structured focal spot achievable with azimuthally polarized light is obtained by placing before the focusing lens a polarizer aligned with the $x$-axis or $y$-axis. This extra optical component leads to a decomposition of the doughnut spot into two half-lobes, vertically or horizontally aligned depending on the polarizer direction, as shown in figure 11. The upper row contains the measured spots, whereas the bottom row contains the simulated ones. Again, the measured immersed and non-immersed focused spots are mapped in a circular measuring window with 2 $\mu$m diameter after being normalized by the maximum intensity value of the immersed spot (on the left-hand side for each case). The measurement results of the immersed spots by the $\mu$-SIL revealed an overall spot-size reduction of approximately 1.3 times in comparison with the non-immersed spot. In a similar way, the peak intensity of the immersed spot was enhanced by a factor of approximately 1.4 times when compared with the non-immersed one. These results are further confirmed by the simulations, where a spot reduction ratio of 1.5 and a peak intensity enhancement ratio of almost 2.1 were found. Such two-lobe spots are particularly interesting for direct-write vortex beam lithography, which can

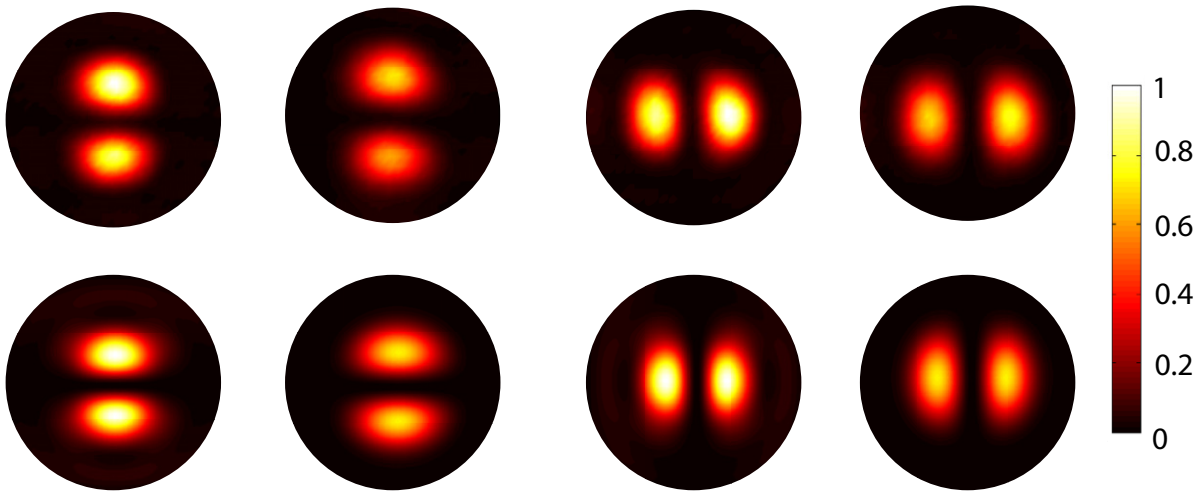


**Figure 11.** Measured and simulated focused intensity distributions of the decomposed azimuthally polarized beam. The top row shows the measured spots, whereas the bottom row contains the simulated spots. The first two columns (left: immersion; and right: non-immersion) were obtained by setting the polarizer aligned with the $x$-axis, while for the remaining spots on the last two columns, the polarizer was aligned with the $y$-axis. A spot-size reduction of approximately 30% was found experimentally. The simulation predicts a maximum reduction of almost 1.5 due to the immersion effect. All intensities are normalized with respect to the peak intensity of the immersed spot. The circular measuring window has 2 $\mu$m diameter.

produce well-separated line patterns of width below 100 nm at visible light illumination. One may also use such beams for spontaneous trapping of two nano-scale particles with 100 nm separation.

### *7.3. The first-order Bessel–Gauss beam*

The last structured spot considered in this work is obtained by placing an annular aperture in the entrance pupil of the high-NA focusing lens, as described before. The resulting focused spot, known as the first-order Bessel–Gauss beam, is characterized by the presence of relatively strong side lobes, as shown in figure 12. In that figure, the spot-size reduction and peak intensity enhancement due to the immersion effect are clearly verified. The unity normalized intensity profiles in the right column confirm the spot size reduction. In fact, a reduction ratio of approximately 1.3 is found in the measurements.

Simulations performed with the azimuthally polarized beam incident on the focusing objective in the presence of the annular aperture confirm the experimental results. As seen in figure 13, the spot-size reduction and peak intensity enhancement are predicted by the simulations. The reduction ratio is again close to the refractive index value of the $\mu$-SIL, namely $n = 1.5$. Interestingly, the maximum intensity enhancement reaches a ratio of almost 3.1, the highest ratio found among all the cases considered here. However, the absolute value of the

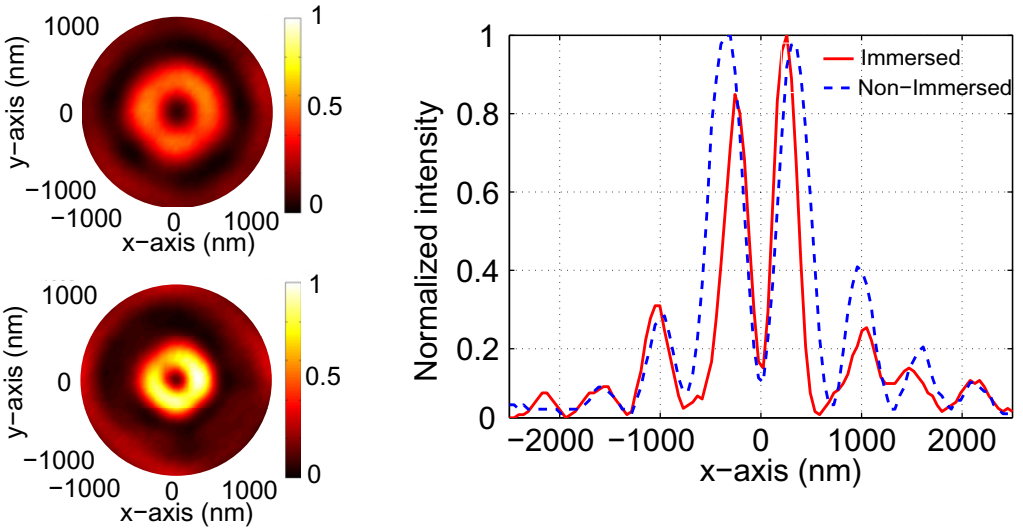


**Figure 12.** Measured intensity distributions of the first-order Bessel–Gauss spots: on the top left, the non-immersed spot is shown. The immersed spot is shown on the bottom left. The intensities are normalized with respect to the peak intensity of the immersion spot. In the right figure, the profiles along the $x$-axis for both spots are plotted after unity normalization. A reduction of the spot size of approximately 30% is achieved due to the immersion lens. The Bessel spots are mapped in a 2 $\mu$m circular measuring window.

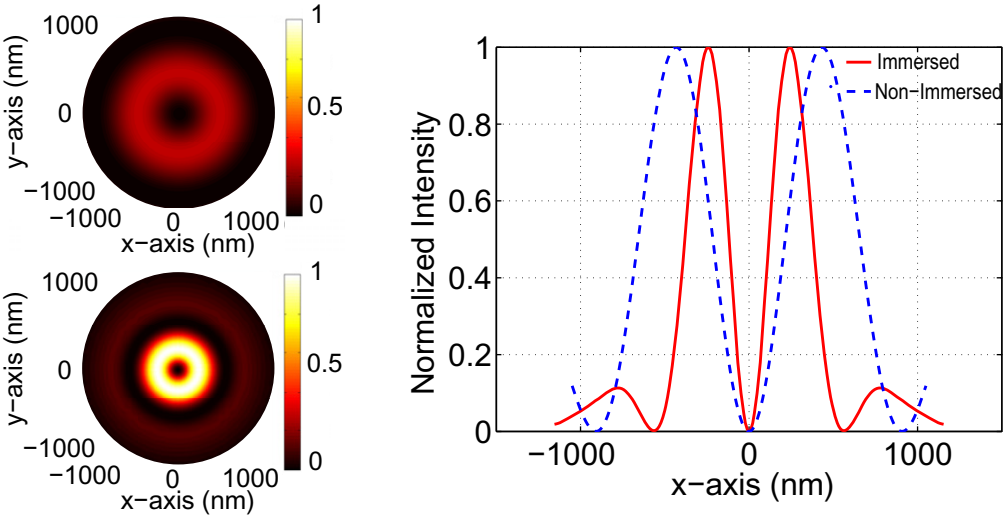


**Figure 13.** Simulated intensity distributions of the first-order Bessel–Gauss focal spots: on the top left, the non-immersed spot is shown, whereas the immersed spot is shown on the bottom left. Intensities are normalized in the same way as in figure 8. A huge peak intensity enhancement of 3.1 times compared with the non-immersed spot is found. On the right, the profiles along the $x$-axis for both spots are plotted after unity normalization. The immersed spot size is again reduced by a factor of 1.5 compared with the non-immersed spot.

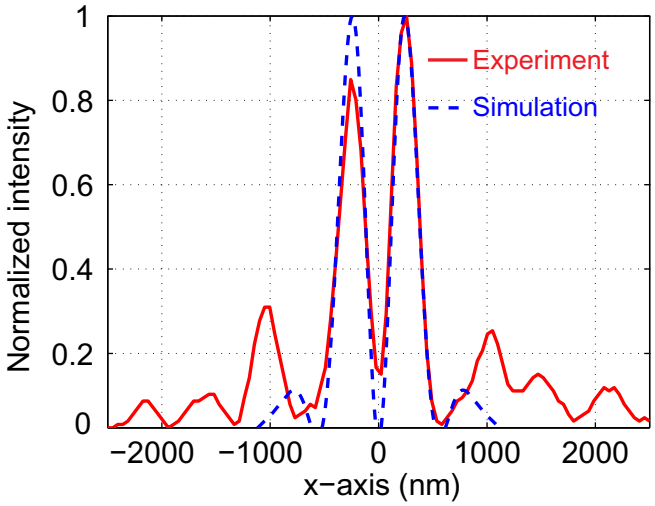


**Figure 14.** Comparison between the measured and the simulated intensity profiles of the immersed first-order Bessel–Gauss spot. The measured central dark region is in good agreement with the simulated spot. All intensities are normalized.

peak intensity in the immersed case is two orders of magnitude smaller than in the other cases. Such reduction in the absolute value is a direct consequence of having 70% of the entrance pupil blocked.

As in the azimuthal doughnut focused spot, the size of the central dark spot is of significant interest. The profile comparison between the measured and the simulated focused spot is shown in figure 14. Good agreement regarding the dark central spot area is found in both cases. The nominal value of the FWHM dark spot in the Bessel spot is 104 nm, approximately 15% smaller than the azimuthal doughnut dark spot. However, the nominal peak intensity in the surrounding ring is two orders of magnitude smaller, which makes the azimuthal doughnut spot preferable over the first-order Bessel–Gauss spot. In the outer part of the spot intensity distribution, a major influence from possible imperfections of the $\mu$-SIL in that region is again noticed. Thus, deviations from the simulated focused spot are found in that region.

## 8. Conclusions

A detailed study of the immersion properties of the 2 $\mu$m diameter $\mu$-SIL was carried out in this work. The generation of a submicron-size doughnut-shape hollow spot was demonstrated, and its properties after being immersed by the $\mu$-SIL were studied. Firstly, the immersion effect was verified by characterizing the spot-size reduction and the peak intensity enhancement of the linearly polarized focal spot at 642 nm wavelength. The spot-size reduction ratio is found to be comparable with the refractive index of the $SiO_2$ SIL ($n = 1.5$) and the peak intensity is increased by a factor of 1.87, which indicates 17% transmission loss. Secondly, the structured immersion beams, e.g. an azimuthally polarized beam, its decompositions and the first-order Bessel–Gauss beam, have been applied to form the doughnut-shape hollow immersion spots. Experiments show good agreement with the rigorous FEM simulations, in particular for the reduction of the dark region of the hollow spots. The FWHM size of such a dark zone is found

to be 220 nm in immersion by the $\mu$-SIL. We assume that the fabrication errors near the rim cause a small discrepancy of the experimental results compared with the numerical results. Since an important feature is the size of the dark zone, such errors near the rim can be neglected in applications. In particular, the central dark region of such a small hollow focal spot is of great interest for optical dark trapping of nano-size particles and vortex beam direct-write lithography.

## Acknowledgments

The research leading to these results has received funding from the European Space Agency and the European Community's Seventh Framework Programme FP7-ICT-2007-2 under grant agreement no. 224226.

## References

[1] Zhan Q 2009 *Adv. Opt. Photon.* **1** 1–57
[2] Brown T G 2011 *Prog. Opt.* **56** 81–129
[3] Descrovi E, Vaccaro L, Aeschimann L, Nakagawa W, Staufer U and Herzig H G 2005 *J. Opt. Soc. Am.* A **22** 1432–41
[4] Dorn R, Quabis S and Leuchs G 2003 *Phys. Rev. Lett.* **91** 233901
[5] Sheppard C J R and Choudhury A 2004 *Appl. Opt.* **43** 4322–7
[6] Wang H, Shi L, Lukyanchuk B, Sheppard C and Chong C T 2008 *Nature Photon.* **2** 501–5
[7] Hell S W and Wichmann J 1994 *Opt. Lett.* **19** 780–2
[8] Fischer J and Wegener M 2011 *Opt. Mater. Express* **1** 614–24
[9] Scott T F, Kowalski B A, Sullivan A C, Bowman C N and McLeod R R 2009 *Science* **15** 913–7
[10] Dienerowitz M, Mazilu M and Dholakia K 2008 *J. Nanophoton.* **2** 021875
[11] Lankers M, Popp J, Urlaub E, Stahl H, Rössling G and Kiefer W 1995 *J. Mol. Struct.* **348** 265–8
[12] Sasaki K, Koshioka M, Misawa H, Kitamura N and Masuhara H 1992 *Appl. Phys. Lett.* **60** 807–9
[13] Davis E J and Schweiger G 2002 *The Airborne Microparticle: Its Physics, Chemistry, Optics and Transport Phenomena* (Berlin: Springer) pp 780–5
[14] Shvedov V G, Desyatnikov A S, Rode A V, Krolikowski W and Kivshar Yu S 2009 *Opt. Express* **17** 5743–57
[15] Shvedov V G, Hnatovsky C, Rode A V and Krolikowski W 2011 *Opt. Express* **19** 17350–6
[16] Chu S 1998 *Rev. Mod. Phys.* **70** 685–706
[17] Isenhower L, Williams W, Dally A and Saffman M 2009 *Opt. Lett.* **34** 1159–61
[18] Xu P, He X, Wang J and Zhan M 2010 *Opt. Lett.* **35** 2164–6
[19] Ganic D, Gan X and Gu M 2003 *Opt. Express* **11** 2747–52
[20] Kang J-H, Kim K, Ee H-S, Lee Y-H, Yoon T-Y, Seo M-K and Park H-G 2011 *Nature Commun.* **2** 582
[21] Braat J 1997 *Appl. Opt* **36** 8459–67
[22] Hooke R 1678 *Lectures and Collections; Microscopium* (London: Royal Society)
[23] Abbe E 1879 *J. R. Microsc. Soc.* **2** 812–24
[24] Mansfield S M and Kino G S 1990 *Appl. Phys. Lett.* **57** 2615
[25] Brunner R, Burkhardt M, Pesch A, Sandfuchs O, Ferstl M, Hohng S and White J O 2004 *J. Opt. Soc. Am.* A **21** 1186–91
[26] Fletcher D A, Crozier K B, Quate C F, Kino G S, Goodson K E, Simanovskii D and Palanker D V 2000 *Appl. Phys. Lett.* **77** 2109
[27] Lang M, Milster T D, Aspnes E, Minamitani T and Borek G 2007 *Japan. J. Appl. Phys.* **46** 3737
[28] Brun M, Richard M and Nicoletti S 2009 *Int. Symp. on Optical Memory* Mo-E-04 pp 56–7
[29] Lee J Y *et al* 2009 *Nature* **460** 498–501
[30] Mason D R, Jouravlev M V and Kim K S 2010 *Opt. Lett.* **35** 2007–9

[31] Kim M-S, Scharf T, Haq M T, Nakagawa W and Herzig H P 2011 *Opt. Lett.* **36** 3930–2
[32] Kim M-S, Scharf T and Herzig H P 2010 *Opt. Express* **18** 14319–29
[33] Kim M-S, Scharf T, Mühlig S, Rockstuhl C and Herzig H G 2011 *Opt. Express* **19** 10206–20
[34] Kim M-S, Scharf T, Menzel C, Rockstuhl C and Herzig H G 2012 *Opt. Express* **20** 4903–20
[35] Rockstuhl C, Märki I, Scharf T, Salt M, Herzig H G and Dändliker R 2006 *Curr. Nanosci.* **2** 337–50
[36] Milione G, Sztul H I, Nolan D A and Alfano R R 2011 *Phys. Rev. Lett.* **107** 053601
[37] Milione G, Evans S, Nolan D A and Alfano R R 2012 *Phys. Rev. Lett.* **108** 190401
[38] Stalder M and Schadt M 1996 *Opt. Lett.* **21** 1948–51
[39] Gori F, Guattari G and Padovani C 1987 *Opt. Commun.* **64** 491–5
[40] Greene P L and Hall D G 1998 *J. Opt. Soc. Am.* A **15** 3020–27
[41] Huang K, Shi P, Cao G W, Li K, Zhang X B and Li Y P 2011 *Opt. Lett.* **36** 888–90
[42] Siegman A E 1986 *Lasers* (Mill Valley, CA: University Science Books) 665
[43] Wachters A J and Urbach H P 2008 *Technical Note Phillips Research Europe* PR-TN 00042
[44] Wei W, Wachters A J and Urbach H P 2007 *J. Opt. Soc. Am.* A **24** 866–81
[45] Monk P 2003 *Finite Element Method for Maxwell's Equations* (Oxford: Oxford Science Publications)
[46] Bahlmann K and Hell S W 2000 *Appl. Phys. Lett.* **77** pp 612–4